How to read optical properties of matter via the Kubo-Greenwood approach

G. S. Demyanov [1], V. B. Fokin [1], D. V. Knyazev [1], D. V. Minakov [1], M. A. Paramonov [1], and P. R. Levashov [1,2,*]

[1]*Joint Institute for High Temperatures, Izhorskaya 13 Building 2, Moscow 125412, Russia*

[2]*Moscow Institute of Physics and Technology, Institutskiy Pereulok 9, Dolgoprudny, Moscow Region 141701, Russia*

Substances with a complex electronic structure exhibit non-Drude optical properties that are challenging to interpret experimentally and theoretically. In our recent paper [Phys. Rev. E **105**, 035307 (2022)], we offered a computational method based on the continuous Kubo-Greenwood formula, which expresses dynamic conductivity as an integral over the electron spectrum. In this Letter, we propose a methodology to analyze the complex conductivity using liquid Zr as an example to explain its nontrivial behavior. To achieve this, we apply the continuous Kubo-Greenwood formula and extend it to include the imaginary part of the complex conductivity into the analysis. Our method is suitable for a wide range of substances, providing an opportunity to explain optical properties from *ab initio* calculations of any difficulty.

Introduction. Optical properties are of great interest for both industrial and fundamental research applications [1–4]. At the dawn of rapid development in quantum mechanics, Drude proposed the electrical conduction theory [5], which is still widely used and evolved [6–8]. Despite its success, the Drude formula (1) fails to describe complicated conductivity curves observed in experiments. Moreover, this formula requires *a posteriori* knowledge of the collision time.

Unfortunately, the experimental analysis of such dependencies is also limited, as the absorption between two energy levels cannot be directly measured [9]. Therefore, the transition intensity is often assumed to be constant [10,11], which is a very rough approximation [12]. The reader can find an overview of different experimental methods to measure the optical properties of metals in Refs. [13–17].

Numerous attempts have been made to unravel optical properties using analytical techniques [18–20], leading to significant advances in our understanding of conductivity theory. However, each material possesses a unique electronic structure that is difficult to capture by analytical methods alone. Consequently, there is an urgent need for a method that not only interprets optical properties qualitatively, but also quantitatively, without relying on tunable parameters.

The advances in solid state physics theory [21] and quantum chemistry [22,23], as well as the implementation of density functional theory (DFT) [24–27], allow to obtain *ab initio* data on the thermodynamical [28–34] and optical properties of matter [35–38]. As a result, a number of powerful research techniques have emerged, including Korringa-Kohn-Rostoker (KKR) [39–41], time-dependent DFT (TD-DFT) [42–45], dynamical mean-field theory (DMFT) [46–48], Boltzmann transport theory [49,50], *GW* method [51,52], and random phase approximation (RPA) [53,54].

The Kubo-Greenwood (KG) formula is one of the commonly used methods for calculating optical properties [55–59]. It allows to obtain the real part of complex conductivity [or the dynamic conductivity $\sigma_1(\omega)$]; its imaginary part [or the imaginary conductivity $\sigma_2(\omega)$] can be obtained from the Kramers-Kronig relation [60]. The electronic structure is calculated by DFT, while the ion dynamics is accounted for by a quantum molecular dynamics (QMD) simulation. Although the implementation of the KG formula in DFT involves approximate Kohn-Sham wave functions, this method produces good results for static and dynamic conductivity, and other optical properties of several substances [61–65].

However, analyzing a final result from the usual KG formula is still challenging, as it involves a discrete sum over all electron transitions. To address this issue, we developed a technique for smoothing the dipole matrix elements squared and obtained the *continuous Kubo-Greenwood* (CKG) formula [66]. It appears that the first derivation of this formula is given in the books of Mott and Davis and Madelung [67,68], although without a specific procedure for application to any real materials. This formula enables a straightforward consideration of electronic transition contributions to conductivity, representing $\sigma_1(\omega)$ as an integral of the product of continuous functions (2). Therefore, the CKG formula provides a useful tool for a comprehensive analysis of the optical properties of matter, even for complicated frequency dependencies.

In this Letter, we analyze the contribution of electron transitions to the CKG formula in order to interpret the dynamic conductivity of liquid Zr. We also develop a similar approach for analyzing the imaginary conductivity, extending our analysis to the full set of optical properties. Thus, our approach enables us to gain a deeper understanding of various features of optical properties.

Computation of electronic structure. A QMD simulation of 250 atoms in a cubic supercell was performed using the VASP package [28] to obtain thermodynamic properties and ionic configurations of Zr [69]. 3000 configurations were generated
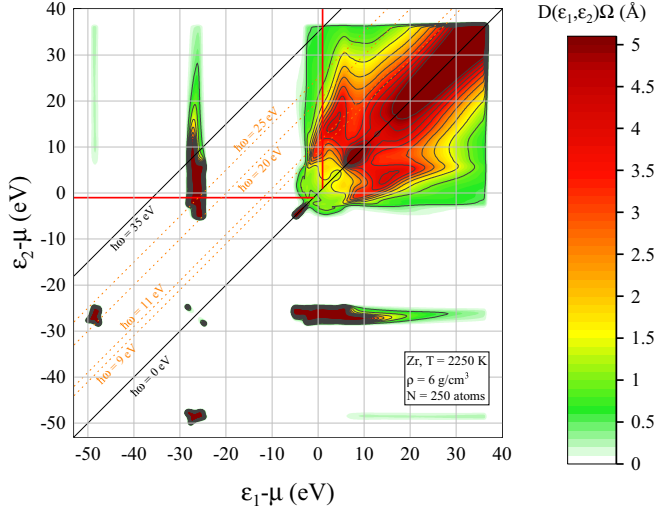
*Corresponding author: pasha@jiht.ru

FIG. 1. SSME, the intensity of transitions between the levels with energies ε_1 and ε_2 multiplied by the system volume Ω. The diagonal lines correspond to some constant frequency $\hbar\omega = \varepsilon_2 - \varepsilon_1$. The vertical and horizontal red lines show the integration region; it arises from the difference of Fermi weights, $[f(\varepsilon_1) - f(\varepsilon_1 + \hbar\omega)]/(\hbar\omega)$.

with a time step of 2 fs. We used the generalized gradient approximation for the exchange-correlation functional in the Perdew-Burke-Ernzerhof parametrization [70] and the projector augmented-wave pseudopotential [71] with 12 valence electrons. We selected specific calculation parameters, including a 400 eV energy cutoff for the plane-wave basis set, a Baldereschi mean-value point [72,73], and 2200 bands, to guarantee the convergence of thermodynamic properties.

Once the system reaches equilibrium after 500 steps, we select a set of five ionic configurations starting from the 600th one in increments of 600. Next, we perform a more precise DFT calculation of the electronic structure via VASP for the selected configurations with 6000 bands total, the same energy cutoff, and a $2 \times 2 \times 2$ **k**-point grid. As a result, we obtain eigenstates, eigenvalues, Fermi weights, and chemical potential μ. Then the averaged over *spatial directions* dipole matrix element squared $D_{ij}^{\mathbf{k}}$ in terms of the momentum operator is computed for all **k** points and bands i, j.

Continuous Kubo-Greenwood formula. The dipole matrix elements squared are not suitable for a direct analysis [66]. For this purpose we use the *smoothed squares of matrix elements* [SSME; see Eqs. (16) and (28) in Ref. [66]]. SSME, $D(\varepsilon_1, \varepsilon_2)$, shows the intensity of the electron transition between the levels with energies ε_1 and ε_2 (see Fig. 1).

The complex electrical conductivity, $\sigma(\omega) = \sigma_1(\omega) + i\sigma_2(\omega)$, is a coefficient of proportionality between the Fourier components of the external electric field and the induced electric current density at a frequency ω. According to Drude, its real, $\sigma_1(\omega)$, and imaginary, $\sigma_2(\omega)$, parts are the following,

$$\sigma_1^{\text{Dr}}(\omega) = \frac{\sigma_{1_{\text{DC}}}^{\text{Dr}}}{1 + \omega^2\tau^2}, \quad \sigma_2^{\text{Dr}}(\omega) = \frac{\sigma_{1_{\text{DC}}}^{\text{Dr}}\omega\tau}{1 + \omega^2\tau^2}$$

$$\sigma_{1_{\text{DC}}}^{\text{Dr}} = \frac{n_e e^2 \tau}{m_e}, \tag{1}$$

where n_e denotes the free-electron density, and τ is the mean free time between ionic collisions. The dynamic conduc-

tivity is obtained from *ab initio* calculations via the CKG formula [66],

$$\sigma_1^{\text{CKG}}(\omega) = \frac{2\pi e^2 \hbar^3}{m_e^2} \int d\varepsilon_1 D(\varepsilon_1, \varepsilon_1 + \hbar\omega)\Omega$$

$$\times \frac{g(\varepsilon_1)g(\varepsilon_1 + \hbar\omega)}{\Omega^2} \frac{f(\varepsilon_1) - f(\varepsilon_1 + \hbar\omega)}{\hbar\omega}, \tag{2}$$

where $g(\varepsilon)$ is the density of states (DOS) and $f(\varepsilon)$ is the Fermi-Dirac distribution. The imaginary conductivity is also obtained in an integral form, $\sigma_2^{\text{CKG}}(\omega) = \int d\varepsilon_1 \sigma_{2,\omega}^{\text{CKG}}(\varepsilon_1)$, from the Kramers-Kronig relation (see the derivation and computational details in the Supplemental Material [74]), where the differential imaginary conductivity

$$\sigma_{2,\omega}^{\text{CKG}}(\varepsilon_1) = \frac{2e^2 \hbar^3}{m_e^2} \frac{g(\varepsilon_1)}{\Omega} \int_0^{+\infty} d(\hbar\nu)D(\varepsilon_1, \varepsilon_1 + \hbar\nu)\Omega$$

$$\times \frac{g(\varepsilon_1 + \hbar\nu)}{\Omega} \frac{f(\varepsilon_1) - f(\varepsilon_1 + \hbar\nu)}{\hbar\nu}$$

$$\times \frac{2\hbar\omega}{(\hbar\omega)^2 - (\hbar\nu)^2}. \tag{3}$$

The integral in Eq. (3) should be understood in the sense of the Cauchy principal value.

It is also convenient to define the following function:

$$D_g(\varepsilon_1, \varepsilon_1 + \hbar\omega) = D(\varepsilon_1, \varepsilon_1 + \hbar\omega)g(\varepsilon_1)g(\varepsilon_1 + \hbar\omega). \tag{4}$$

$D_g(\varepsilon_1, \varepsilon_1 + \hbar\omega)d\varepsilon_1 \, d(\hbar\omega)$ represents the sum of all electron transitions with a frequency ω from some initial energy level ε_1.

The CKG formula (2) has a clear physical meaning. SSME, $D(\varepsilon_1, \varepsilon_1 + \hbar\omega)$, shows the intensity of an electron transition from the initial energy level ε_1 to the final one, $\varepsilon_1 + \hbar\omega$. The DOS product shows the number of energy levels on the initial level $g(\varepsilon_1)$ and on the final level $g(\varepsilon_1 + \hbar\omega)$. The difference between the Fermi weights, $[f(\varepsilon_1) - f(\varepsilon_1 + \hbar\omega)]/(\hbar\omega)$, reflects the occupation of the levels. Finally, the integration over the energy range takes into account the transitions from all the initial energy levels to obtain $\sigma_1^{\text{CKG}}(\omega)$. Note that the difference of Fermi weights limits the integration range in Eq. (2); a transition may occur only from an occupied to unoccupied level (the occupation can be partial).

For the imaginary part $\sigma_2^{\text{CKG}}(\omega)$, all possible transitions from the energy level ε_1 contribute to $\sigma_{2,\omega}^{\text{CKG}}(\varepsilon_1)$ [see Eq. (3)]. The contribution of each transition is determined by several factors, including its intensity, $D(\varepsilon_1, \varepsilon_1 + \hbar\nu)$, the number of levels at the initial, $g(\varepsilon_1)$, and final values, $g(\varepsilon_1 + \hbar\nu)$, the occupancy $[f(\varepsilon_1) - f(\varepsilon_1 + \hbar\nu)]/(\hbar\nu)$, and the "weight" $2\hbar\omega/[(\hbar\omega)^2 - (\hbar\nu)^2]$. To obtain the differential imaginary conductivity $\sigma_{2,\omega}^{\text{CKG}}(\varepsilon_1)$, we sum over all such contributions by integration over $\hbar\nu$ [see Eq. (3)]. Next, we account for the transitions from all initial levels ε_1 by integrating over the electron spectrum to calculate $\sigma_2^{\text{CKG}}(\omega)$.

The calculation of SSME, DOS, $\sigma_1^{\text{CKG}}(\omega)$, $\sigma_{2,\omega}^{\text{CKG}}(\varepsilon_1)$, and $\sigma_2^{\text{CKG}}(\omega)$ is provided via the CUBOGRAM code [66].

While being computationally more expensive, the continuous KG formula (2) allows for a more comprehensive analysis of contributions into $\sigma_1^{\text{CKG}}(\omega)$, compared to the standard KG formula [75]. This can be achieved by examination
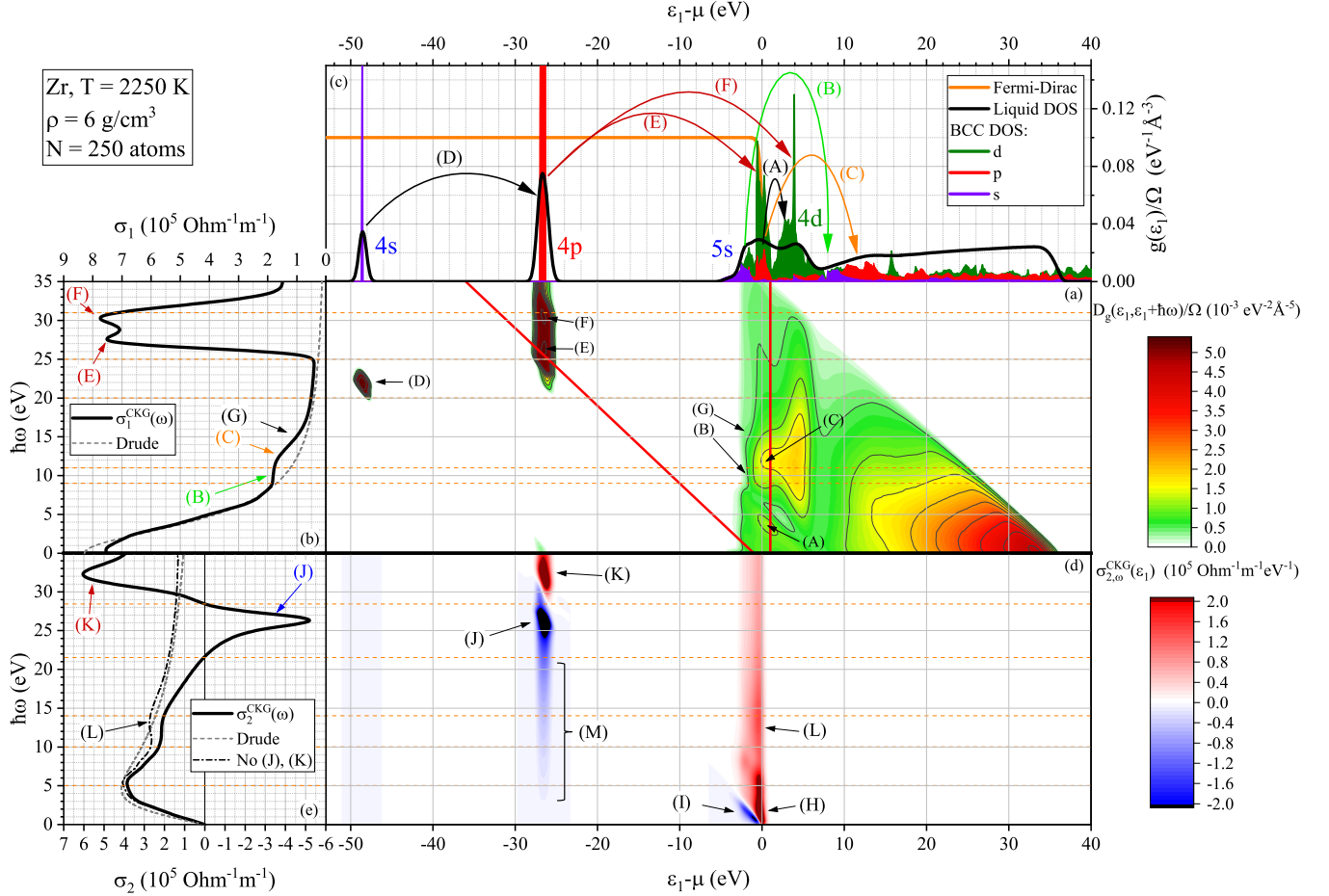
FIG. 2. Analysis of contributions to the real and imaginary parts of complex conductivity. The horizontal axis in (a) and (d) represents the energy of the initial level, and the vertical axis indicates the transition frequency. (a) The product of the transition intensity $D(\varepsilon_1, \varepsilon_1 + \hbar\omega)$ and the number of levels at the initial energy $g(\varepsilon_1)$ and final energy $g(\varepsilon_1 + \hbar\omega)$ divided by the system volume Ω. The vertical and diagonal red lines mark the integration region, which arises from the difference of the Fermi weights, $[f(\varepsilon_1) - f(\varepsilon_1 + \hbar\omega)]/(\hbar\omega)$, and corresponds to the red lines in Fig. 1. (b) The dynamic conductivity, calculated via the CKG formula (2). The gray dashed line shows the Drude fit (1) of the initial segment of $\sigma_1^{\mathrm{CKG}}(\omega)$ with $\sigma_{1_{\mathrm{DC}}}^{\mathrm{Dr}} = 8.3 \times 10^5$ Ohm^{-1} m^{-1} and $\tau/\hbar = 0.22$ eV^{-1}. (c) DOS, $g(\varepsilon_1)$, for electrons at the initial energy level ε_1. The projected DOS, obtained from the decomposition of the wave functions by spherical harmonics, for the bcc lattice at the same density is also shown in (c); it displays DOS for s, p, and d orbitals. (d) The differential imaginary conductivity $\sigma_{2,\omega}^{\mathrm{CKG}}(\varepsilon_1)$ [see Eq. (3)] obtained from the Kramers-Kronig relation. (e) The imaginary conductivity $\sigma_2^{\mathrm{CKG}}(\omega)$ obtained by integrating the differential one. The gray dashed line shows the Drude fit (1); the black dash-dotted line shows the imaginary conductivity without the contribution from inner electrons. Each label in (a)–(c) corresponds to an electron transition from the initial level with energy ε_1 by $\hbar\omega$ eV; labels in (d) and (e) indicate corresponding peaks on $\sigma_{2,\omega}^{\mathrm{CKG}}(\varepsilon_1)$ and $\sigma_2^{\mathrm{CKG}}(\omega)$; their physical meaning differs from that in (a)–(c). The horizontal orange dashed lines show the contribution of transitions for a frequency $\hbar\omega$; any vertical slice represents the contribution of transitions for a given initial energy level ε_1.

of $D(\varepsilon_1, \varepsilon_2)$, $g(\varepsilon)$, and the difference of Fermi weights. Note that the usual and continuous KG formulas are independent implementations of the exact KG formula (see Sec. IV of Ref. [66]).

All quantities such as DOS, SSME, $D_g(\varepsilon_1, \varepsilon_1 + \hbar\omega)$, $\sigma_{2,\omega}^{\mathrm{CKG}}(\varepsilon_1)$, and $\sigma^{\mathrm{CKG}}(\omega)$ are averaged over the set of five ionic configurations.

Contributions to optical properties. In our recent publication [76], we examined the optical properties of liquid Zr at $T = 2250$ K and $\rho = 6$ g/cm^3, calculated using the GREEKUP code [75] that implements the usual KG formula to obtain $\sigma_1^{\mathrm{KG}}(\omega)$ and $\sigma_2^{\mathrm{KG}}(\omega)$.

In our study [76] of $\sigma_1^{\mathrm{KG}}(\omega)$ and $\sigma_2^{\mathrm{KG}}(\omega)$ curves, we observed two specific patterns, which are highly different from the Drude approximation (1) [see Figs. 2(b) and 2(e)].

Following the initial (Drude-like) section of the dynamic conductivity [see Fig. 2(b)], we observed a plateau in the range of $\hbar\omega \in (9, 11)$ eV. In the range of $\hbar\omega \in (25, 33)$ eV we noted a significant hump, which we attribute to the excitation of $4p$ electrons.

The initial section of the imaginary conductivity exhibits the Drude-like behavior too [see Fig. 2(e)]. However, a plateau is also observed in the region of $\hbar\omega \in (10, 13)$ eV. Two sharp humps appear: a negative peak at $\hbar\omega \in (22, 28)$ eV and a positive one at $\hbar\omega \in (28, 35)$ eV. Note that the decay of $\sigma_2^{\mathrm{CKG}}(\omega)$ from its maximum at $\hbar\omega = 5$ eV is more abrupt than that the Drude formula (1) predicts.

To understand such complicated behavior of $\sigma_1^{\mathrm{CKG}}(\omega)$, $\sigma_2^{\mathrm{CKG}}(\omega)$, we need to analyze the intensity of electron transitions $D(\varepsilon_1, \varepsilon_2)$ (see Fig. 1).

The red lines in Fig. 1 indicate the integration region, which arises from the difference of Fermi weights in Eq. (2). Therefore, only the upper left-hand corner of Fig. 1 between the two red lines contributes into $\sigma^{\mathrm{CKG}}(\omega)$. This region includes the areas of high (red), medium (yellow and orange), and low (green) intensity of transitions.

The primary contribution to $\sigma_1^{\mathrm{CKG}}(\omega)$ for transitions at $\hbar\omega < 25$ eV is made up by the upper right-hand corner of Fig. 1 with an initial energy $\varepsilon_1 - \mu > -4$ eV. Although the lower left-hand corner presents the intensity of transitions from $\varepsilon_1 - \mu = -50$ eV to $\varepsilon_2 - \mu \approx -30$ eV, it is outside the integration region and contributes nothing to $\sigma^{\mathrm{CKG}}(\omega)$.

There are, however, transitions from $\varepsilon_1 - \mu \approx -30$ eV to $\varepsilon_2 - \mu > 0$ in the integration region. Due to these transitions, we observe a significant hump on $\sigma_1^{\mathrm{CKG}}(\omega)$ in the range of $\hbar\omega \in (25, 33)$ eV [see Fig. 2(b)]. For the same reason, two peaks appear on $\sigma_2^{\mathrm{CKG}}(\omega)$ in the region $\hbar\omega \in (22, 35)$ eV.

Figure 1 contains the diagonal lines that indicate transitions at a specific frequency, $\varepsilon_2 = \varepsilon_1 + \hbar\omega$. Thus, $D(\varepsilon_1, \varepsilon_1 + \hbar\omega)$ represents the intensity of transitions from the initial energy level ε_1 by the frequency $\hbar\omega$. To visualize it from Fig. 1, we consider the isosceles trapezoid bounded by the black diagonal lines in Fig. 1 and rotate it by $45°$. Then, we shift the upper boundary to the left to form a right trapezoid, which results in Fig. 2(a). Note that Fig. 2(a) shows the transition intensity $D(\varepsilon_1, \varepsilon_1 + \hbar\omega)$ multiplied by the DOS at the initial energy level $g(\varepsilon_1)$ and at the final energy level $g(\varepsilon_1 + \hbar\omega)$. This product is denoted by $D_g(\varepsilon_1, \varepsilon_1 + \hbar\omega)$ [see Eq. (4)].

After calculating all the contributions to $\sigma_1^{\mathrm{CKG}}(\omega)$, we can now compute $\sigma_{2,\omega}^{\mathrm{CKG}}(\varepsilon_1)$. To evaluate this function for a given energy ε_1 and frequency ω, we consider all possible transitions from the level with energy ε_1, denoted by $D_g(\varepsilon_1, \varepsilon_1 + \hbar\nu)$, as shown in Fig. 2(a). These transitions have different "weights" given by $2\hbar\omega[(\hbar\omega)^2 - (\hbar\nu)^2]^{-1}$, and we need to sum over them, according to the occupation of levels, $[f(\varepsilon_1) - f(\varepsilon_1 + \hbar\nu)]/(\hbar\nu)$ [see Eq. (3)]. Figuratively speaking, this process is similar to smearing Fig. 2(a) along the frequency axis using a procedure described by Eq. (3), much like spreading butter on bread, resulting in Fig. 2(d). By integrating this diagram for a fixed frequency $\hbar\omega$ along the energy axis ε_1, we obtain the imaginary conductivity $\sigma_2^{\mathrm{CKG}}(\omega)$.

For clarity, we linked the top energy axis to the DOS in Fig. 2(c), $g(\varepsilon_1)$, and the frequency axis to the dynamic conductivity in Fig. 2(b), $\sigma_1^{\mathrm{CKG}}(\omega)$. The bottom energy axis is linked with Fig. 2(d) of $\sigma_{2,\omega}^{\mathrm{CKG}}(\varepsilon_1)$; its frequency axis is linked to the imaginary conductivity in Fig. 2(e).

Figure 2(a) contains different letter labels (A, B, C, etc.) with coordinates $(\varepsilon_1, \hbar\omega)$. Each label corresponds to a specific transition, which is shown by an arrow in Fig. 2(c). The origin of the arrow indicates the initial electron energy ε_1 while its end points to the final energy $\varepsilon_1 + \hbar\omega$. Hence, the difference between the end and origin of the arrow is the transition frequency $\hbar\omega$.

Next, we analyze contributions to the dynamic conductivity $\sigma_1^{\mathrm{CKG}}(\omega)$.

The first peak in $D_g(\varepsilon_1, \varepsilon_1 + \hbar\omega)$ [labeled (A)] corresponds to the transition of electrons with the initial energy near the chemical potential, $\varepsilon_1 - \mu = 0$, by $\hbar\omega = 3$ eV. Since most of the unoccupied states at $\varepsilon_1 - \mu = 3$ eV correspond to

d orbitals, the peak (A) corresponds to the $p \rightarrow d$ transition in the region $\varepsilon_1 - \mu > 0$.

In the region $\varepsilon_1 - \mu \geqslant 9$ eV, DOS increases, indicating the presence of levels available for transitions from the chemical potential region. This increase in DOS is reflected in the appearance of a peak, labeled (C), which indicates the transitions from the first peak on the d-electron DOS. These transitions cause a non-Drude behavior of the conductivity curve in the range $9 \leqslant \hbar\omega \leqslant 20$ eV, preventing the curve to decrease monotonously.

Consider the region $9 \leqslant \hbar\omega \leqslant 11$ eV [label (B)], highlighted by the dashed orange lines in Fig. 2(a). We observe that in this region, $D_g(\varepsilon_1, \varepsilon_1 + \hbar\omega)$ varies very little with frequency, though it slightly increases (consider the trapezoid limited by orange and red lines). However, this increase is fully compensated by the multiplier $1/(\hbar\omega)$, which weakly decreases in the range from 9 to 11 eV. Consequently, the integrand function in Eq. (2) exhibits a weak frequency dependence, and the energy integral is also weakly frequency dependent. Therefore, the $\sigma_1^{\mathrm{CKG}}(\omega)$ curve shows a plateau in the $\hbar\omega \in (9, 11)$ eV region.

When the frequency increases ($\hbar\omega > 11$ eV), there is a decrease in $D_g(\varepsilon_1, \varepsilon_1 + \hbar\omega)$ [label (G)]. It results in a decrease in $\sigma_1^{\mathrm{CKG}}(\omega)$ within the region of $11 \leqslant \hbar\omega \leqslant 20$ eV. In the range $20 \leqslant \hbar\omega \leqslant 25$ eV, the conductivity shows a Drude-like behavior again.

We observe a peak on $D_g(\varepsilon_1, \varepsilon_1 + \hbar\omega)$ corresponding to $4s \rightarrow 4p$ transitions [labeled as (D)] at $\hbar\omega = 22$ eV. However, despite the presence of this peak, these transitions do not occur due to the levels being fully occupied, which we have also noted in Fig. 1.

Consider now the region of the double peak on the conductivity, which is labeled as (E) and (F), at $25 \leqslant \hbar\omega \leqslant 31$ eV. These peaks are the result of intensive transitions from the inner $4p$ electrons to $4d$. Note that the intensity of the double peak in the conductivity follows from that of the double peak in the projected DOS of d electrons, in the vicinity of the chemical potential. However, SSME (see Fig. 1) in this region shows no splitting into two peaks.

Following the peak (F), we see a sharp drop in $D_g(\varepsilon_1, \varepsilon_1 + \hbar\omega)$ as $g(\varepsilon_2)$ at $\varepsilon_2 - \mu = -27 + \hbar\omega = 8$ eV for $\hbar\omega = 35$ eV decreases sharply. This is also reflected by a sharp decrease of the peak (F) on the function $D_g(\varepsilon_1, \varepsilon_1 + \hbar\omega)$, and hence a sharp decrease of the conductivity $\sigma_1^{\mathrm{CKG}}(\omega)$.

Next, we analyze contributions to the imaginary conductivity $\sigma_2^{\mathrm{CKG}}(\omega)$ [see Figs. 2(d) and 2(e)].

Let us begin by examining the excitation region of the inner $4p$ electrons (-30 eV $\leqslant \varepsilon_1 - \mu \leqslant -23$ eV). These excitations have different signs for various $\hbar\omega$: A negative peak (J) and a positive peak (K) are observed, which arise as a result of transitions (E) and (F). The peak (J) has a very long tail [see label (M)]. Therefore, in contrast to $\sigma_1^{\mathrm{CKG}}(\omega)$, the impact of these deep $4p$ electron excitations is noticeable in $\sigma_2^{\mathrm{CKG}}(\omega)$ even for relatively low $\hbar\omega \leqslant 20$ eV. To demonstrate it, we computed the curve $\sigma_2^{\mathrm{CKG}}(\omega)$ excluding the spectrum part of $\varepsilon_1 - \mu \leqslant -10$ eV [see Fig. 2(e), black dash-dotted line]. Consequently, peaks (J) and (K) disappear, and this curve becomes similar to the Drude one.

Next, we focus on the transitions from levels near the chemical potential. The sum of all transitions from the level

$\varepsilon_1 = \mu$ is positive, as indicated by peak (H). This peak (H) leads to a significant increase in $\sigma_2^{\text{CKG}}(\omega)$ for $\hbar\omega \leqslant 5$ eV. However, in the same frequency range, transitions from levels -4 eV $\leqslant \varepsilon_1 - \mu \leqslant -0.5$ eV contribute negatively, as demonstrated by peak (I). This peak (I) results in a slower increase in $\sigma_2^{\text{CKG}}(\omega)$ compared to the Drude curve $\sigma_2^{\text{Dr}}(\omega)$ for $\hbar\omega \leqslant 5$ eV.

In the region $\hbar\omega \in (5, 10)$ eV, there are no negative contributions near the chemical potential, and peak (H) decreases, leading to a decrease in $\sigma_2^{\text{CKG}}(\omega)$. The curve $\sigma_{2,\omega}^{\text{CKG}}(\mu)$ exhibits a slight increase for $\hbar\omega \in (10, 14)$ eV, as illustrated by peak (L). It causes a small increase in the imaginary conductivity curve [the one without peaks (J) and (K)]. However, the negative effect of transitions from inner $4p$ levels compensates this increase, resulting in a plateau on $\sigma_2^{\text{CKG}}(\omega)$ for $\hbar\omega \in (10, 14)$ eV. As the positive contribution near the chemical potential decreases and the negative one from $4p$ electrons increases, $\sigma_2^{\text{CKG}}(\omega)$ drops sharply after the plateau for $\hbar\omega \in (14, 21)$ eV.

Through the analysis of SSME, $D(\varepsilon_1, \varepsilon_2)$, and $D_g(\varepsilon_1, \varepsilon_1 + \hbar\omega)$, along with the projected DOS, we have successfully explained the nontrivial behavior in the complex conductivity of liquid Zr. It is our expectation that such an analysis will facilitate the interpretation of the optical properties of other substances with a non-Drude behavior.

Conclusion. The interpretation of optical properties is crucial for understanding the electronic structure of matter. However, there is often a lack of such data, and their analysis can be challenging due to limitations in measuring the intensity of electron transitions. *Ab initio* calculations using the Kubo-Greenwood formula provide a solution to these problems, yielding accurate predictions of optical and transport properties that are consistent with experimental data. However, to explain these complicated dependencies, it is crucial to apply the continuous Kubo-Greenwood formula, which represents complex conductivity in an integral form.

In our work, we demonstrate the power of this formula to study the complex conductivity of liquid Zr, revealing its nontrivial behavior. This approach can be used to interpret the optical properties of complex substances obtained from electronic structure calculations.

---

[1] J. P. Santos Pires, S. M. João, A. Ferreira, B. Amorim, and J. M. Viana Parente Lopes, Phys. Rev. Lett. **129**, 196601 (2022).

[2] B. B. L. Witte, L. B. Fletcher, E. Galtier, E. Gamboa, H. J. Lee, U. Zastrau, R. Redmer, S. H. Glenzer, and P. Sperling, Phys. Rev. Lett. **118**, 225001 (2017).

[3] M. E. Povarnitsyn, P. R. Levashov, and D. V. Knyazev, Appl. Phys. Lett. **112**, 051603 (2018).

[4] A. Kietzmann, R. Redmer, M. P. Desjarlais, and T. R. Mattsson, Phys. Rev. Lett. **101**, 070401 (2008).

[5] P. Drude, Ann. Phys. **306**, 566 (1900).

[6] A. Urichuk, A. Klümper, and J. Sirker, Phys. Rev. Lett. **129**, 096602 (2022).

[7] H. Singh, R. Vasseur, and S. Gopalakrishnan, Phys. Rev. Lett. **130**, 046001 (2023).

[8] O. E. Raichev, Phys. Rev. Lett. **120**, 146802 (2018).

[9] W. B. Jackson, S. M. Kelso, C. C. Tsai, J. W. Allen, and S.-J. Oh, Phys. Rev. B **31**, 5187 (1985).

[10] G. Cody, in *Hydrogenated Amorphous Silicon*, edited by J. I. Pankove, Semiconductors and Semimetals Vol. 21 (Elsevier, Amsterdam, 1984), pp. 11–82.

[11] M. H. Cohen, C. M. Soukoulis, and E. N. Economou, AIP Conf. Proc. **120**, 371 (1984).

[12] S. Abe and Y. Toyozawa, J. Phys. Soc. Jpn. **50**, 2185 (1981).

[13] V. Sobolev, Database of Thermophysical Properties of Liquid Metal Coolants for GEN-IV, Technical Report No. BLG-1069, Belgian Nuclear Research Center (2011), https://inis.iaea.org/collection/NCLCollectionStore/_Public/43/095/43095088.pdf.

[14] M. Bass, C. DeCusatis, J. Enoch, V. Lakshminarayanan, G. Li, C. MacDonald, V. Mahajan, and E. Van Stryland, *Handbook of Optics, Volume IV: Optical Properties of Materials, Nonlinear Optics, Quantum Optics*, 3rd ed. (McGraw-Hill, New York, 2009).

[15] J. C. Miller, Philos. Mag. **20**, 1115 (1969).

[16] N. R. Comins, Philos. Mag. **25**, 817 (1972).

[17] N. Smith, Adv. Phys. **16**, 629 (1967).

[18] A. Sommerfeld, Z. Phys. **47**, 1 (1928).

[19] N. F. Mott and C. Zener, Math. Proc. Cambridge Philos. Soc. **30**, 249 (1934).

[20] J. M. Ziman, Philos. Mag. **6**, 1013 (1961).

[21] N. W. Ashcroft and N. D. Mermin, *Solid State Physics* (Harcourt College Publishers, New York, 1976).

[22] N. Marzari, A. A. Mostofi, J. R. Yates, I. Souza, and D. Vanderbilt, Rev. Mod. Phys. **84**, 1419 (2012).

[23] Y. Shao, L. F. Molnar, Y. Jung, J. Kussmann, C. Ochsenfeld, S. T. Brown, A. T. Gilbert, L. V. Slipchenko, S. V. Levchenko, D. P. O'Neill *et al.*, Phys. Chem. Chem. Phys. **8**, 3172 (2006).

[24] P. Hohenberg and W. Kohn, Phys. Rev. **136**, B864 (1964).

[25] W. Kohn and L. J. Sham, Phys. Rev. **140**, A1133 (1965).

[26] M. Levy, Proc. Natl. Acad. Sci. USA **76**, 6062 (1979).

[27] E. H. Lieb, Density functionals for Coulomb systems, in *Inequalities: Selecta of Elliott H. Lieb*, edited by M. Loss and M. B. Ruskai (Springer, Berlin, 1983), pp. 269–303.

[28] G. Kresse and J. Hafner, Phys. Rev. B **47**, 558 (1993).

[29] B. Holst, R. Redmer, and M. P. Desjarlais, Phys. Rev. B **77**, 184201 (2008).

[30] D. V. Minakov, M. A. Paramonov, and P. R. Levashov, Phys. Rev. B **103**, 184204 (2021).

[31] J. Clérouin, P. Renaudin, and P. Noiret, Phys. Rev. E **77**, 026409 (2008).

[32] D. V. Minakov and P. R. Levashov, J. Phys.: Conf. Ser. **946**, 012093 (2018).

[33] D. Li, H. Liu, S. Zeng, C. Wang, Z. Wu, P. Zhang, and J. Yan, Sci. Rep. **4**, 5898 (2014).

[34] D. V. Minakov, M. A. Paramonov, and P. R. Levashov, High Temp. - High Pressures **49**, 211 (2020).

[35] R. Redmer, Phys. Rev. E **59**, 1073 (1999).

[36] M. P. Desjarlais, J. D. Kress, and L. A. Collins, Phys. Rev. E **66**, 025401(R) (2002).

[37] D. V. Knyazev and P. R. Levashov, Phys. Plasmas **23**, 102708 (2016).

[38] D. V. Knyazev and P. R. Levashov, Phys. Plasmas **21**, 073302 (2014).

[39] J. Xu, P. Zhang, K. Haule, J. Minar, S. Wimmer, H. Ebert, and R. E. Cohen, Phys. Rev. Lett. **121**, 096601 (2018).

[40] J. Korringa, Physica **13**, 392 (1947).

[41] W. Kohn and N. Rostoker, Phys. Rev. **94**, 1111 (1954).

[42] K. Ramakrishna, M. Lokamani, A. Baczewski, J. Vorberger, and A. Cangi, Phys. Rev. B **107**, 115131 (2023).

[43] X. Andrade, S. Hamel, and A. A. Correa, Eur. Phys. J. B **91**, 229 (2018).

[44] Z. A. Moldabekov, M. Pavanello, M. P. Böhme, J. Vorberger, and T. Dornheim, Phys. Rev. Res. **5**, 023089 (2023).

[45] E. Runge and E. K. U. Gross, Phys. Rev. Lett. **52**, 997 (1984).

[46] G. Kotliar, S. Y. Savrasov, K. Haule, V. S. Oudovenko, O. Parcollet, and C. A. Marianetti, Rev. Mod. Phys. **78**, 865 (2006).

[47] L. V. Pourovskii, J. Mravlje, M. Pozzo, and D. Alfè, Nat. Commun. **11**, 4105 (2020).

[48] A. Georges, G. Kotliar, W. Krauth, and M. J. Rozenberg, Rev. Mod. Phys. **68**, 13 (1996).

[49] N. A. Smirnov, Phys. Rev. B **106**, 024109 (2022).

[50] P. B. Allen, Phys. Rev. B **17**, 3725 (1978).

[51] F. Aryasetiawan and O. Gunnarsson, Rep. Prog. Phys. **61**, 237 (1998).

[52] L. Reining, WIREs Comput. Mol. Sci. **8**, e1344 (2018).

[53] V. I. Gavrilenko and F. Bechstedt, Phys. Rev. B **55**, 4343 (1997).

[54] D. Pines, in *Solid State Physics*, edited by F. Seitz and D. Turnbull (Academic, New York, 1955), Vol. 1, pp. 367–450.

[55] T. R. Mattsson and M. P. Desjarlais, Phys. Rev. Lett. **97**, 017801 (2006).

[56] A. Kietzmann, B. Holst, R. Redmer, M. P. Desjarlais, and T. R. Mattsson, Phys. Rev. Lett. **98**, 190602 (2007).

[57] J. Clérouin, C. Starrett, G. Faussurier, C. Blancard, P. Noiret, and P. Renaudin, Phys. Rev. E **82**, 046402 (2010).

[58] J.-A. Korell, M. French, G. Steinle-Neumann, and R. Redmer, Phys. Rev. Lett. **122**, 086601 (2019).

[59] X.-W. Zhang, H. Chen, E.-G. Wang, J. Shi, and X.-Z. Li, Phys. Rev. B **105**, 155148 (2022).

[60] B. Y. Hu, Am. J. Phys. **57**, 821 (1989).

[61] S. Mazevet, J. Clérouin, V. Recoules, P. M. Anglade, and G. Zerah, Phys. Rev. Lett. **95**, 085002 (2005).

[62] D. Knyazev and P. Levashov, Comput. Mater. Sci. **79**, 817 (2013).

[63] B. Holst, V. Recoules, S. Mazevet, M. Torrent, A. Ng, Z. Chen, S. E. Kirkwood, V. Sametoglu, M. Reid, and Y. Y. Tsui, Phys. Rev. B **90**, 035121 (2014).

[64] Z. Chen, B. Holst, S. E. Kirkwood, V. Sametoglu, M. Reid, Y. Y. Tsui, V. Recoules, and A. Ng, Phys. Rev. Lett. **110**, 135001 (2013).

[65] M. French, M. Bethkenhagen, A. Ravasio, and J.-A. Hernandez, Phys. Rev. B **107**, 134109 (2023).

[66] G. S. Demyanov, D. V. Knyazev, and P. R. Levashov, Phys. Rev. E **105**, 035307 (2022).

[67] N. F. Mott and E. A. Davis, *Electronic Processes in Non-Crystalline Materials*, 2nd ed. (Clarendon, Oxford, U.K., 1979).

[68] O. Madelung, *Introduction to Solid-State Theory*, Springer Series in Solid-State Sciences (Springer, Berlin, 1997).

[69] M. A. Paramonov, D. V. Minakov, V. B. Fokin, D. V. Knyazev, G. S. Demyanov, and P. R. Levashov, J. Appl. Phys. **132**, 065102 (2022).

[70] J. P. Perdew, K. Burke, and M. Ernzerhof, Phys. Rev. Lett. **77**, 3865 (1996).

[71] G. Kresse and D. Joubert, Phys. Rev. B **59**, 1758 (1999).

[72] A. Baldereschi, Phys. Rev. B **7**, 5212 (1973).

[73] D. V. Minakov, M. A. Paramonov, and P. R. Levashov, AIP Adv. **8**, 125012 (2018).

[74] See Supplemental Material at http://link.aps.org/supplemental/10.1103/PhysRevE.108.L053301 for details of the derivation and computation of the imaginary conductivity.

[75] D. Knyazev and P. Levashov, Contrib. Plasma Phys. **59**, 345 (2019).

[76] V. Fokin, D. Minakov, and P. Levashov, Symmetry **15**, 48 (2023).